DOI: 10.1002/ ((please add manuscript number))

Article type: Full Paper

Toward high thermoelectric performance large-size nanostructured BiSbTe alloys via optimization of sintering temperature distribution

Gang Zheng, Xianli Su, Xinran Li, Tao Liang, Hongyao Xie, Xiaoyu She, Yonggao Yan, Ctirad Uher, Mercouri G. Kanatzidis, Xinfeng Tang**

G. Zheng, X. L. Su, X. R. Li, T. Liang, H. Y. Xie, X. Y. She, Y. G. Yan, Prof. X. F. Tang

State Key Laboratory of Advanced Technology for Materials Synthesis and Processing, Wuhan University of Technology, Wuhan 430070, China
E-mail: suxianli@whut.edu.cn; tangxf@whut.edu.cn

Prof. C. Uher
Department of Physics, University of Michigan, Ann Arbor, Michigan 48109, USA

Prof. M. G. Kanatzidis
Department of Chemistry, Northwestern University, Evanston, Illinois 60208, USA

This is the author manuscript accepted for publication and has undergone full peer review but has not been through the copyediting, typesetting, pagination and proofreading process, which may lead to differences between this version and the Version of Record. Please cite this article as doi: 10.1002/aenm.201600595.

This article is protected by copyright. All rights reserved.

Keywords: Thermoelectric, large-size, nanostructure, homogeneity

High thermoelectric performance of mechanically robust p-type Bi_2Te_3-based materials prepared by melt-spinning (MS) combined with plasma activated sintering (PAS) method can be obtained with small, laboratory grown samples. However, large-size samples are required for commercial applications. Here, large-size p-type Bi_2Te_3-based ingots with 30 mm, 40 mm, 60 mm in diameter were produced by MS-PAS, and the influence of temperature distribution during the sintering process on the composition and thermoelectric properties was systematically studied for the first time. Room temperature Scanning Seebeck Microprobe results show that the large size ingot is inhomogeneous, induced by ellipsoidal shape distributed temperature field during the sintering process, which is verified by the finite element analysis. Although some temperature differences are unavoidable in the sintering process, homogeneity and mechanical properties of ingots can be improved by appropriately extending the sintering time and design of graphite die. Samples cut from ingots attained the peak *ZT* value of 1.15 at 373 K, about 17% enhancement over commercial zone-melted samples. Moreover, the compressive and bending strengths were improved by several times as well. It is important to ascertain that large-size p-type Bi_2Te_3-based thermoelectric materials with high thermoelectric performance can be fabricated by MS-PAS.

1. Introduction

Thermoelectricity has attracted a worldwide interest in the past decades as a means to directly convert heat into electricity. It is potentially a reliable vibration-free technology with indirect environmental benefits as well.[1,2] However, large scale commercialization of thermoelectric power generators is still in its infancy mainly for two reasons: (a) the conversion efficiency of commercially available materials is not high enough as measured by the dimensionless figure of merit *ZT* defined as $ZT=\alpha^2\sigma T/\kappa$, where α, σ, κ and T are the Seebeck coefficient, the electrical conductivity, the thermal conductivity, and the absolute temperature, respectively.[3] (b) difficulties with reproducible

This article is protected by copyright. All rights reserved.

large-scale fabrication of high performance thermoelectric materials that also possess robust mechanical properties.

Bi_2Te_3-based compounds have been, by far, the leading state-of-the-art thermoelectric material for near room temperature applications with the peak *ZT* value of about unity. Commercial Bi_2Te_3-based materials are typically prepared by zone melting (ZM) and have favorable thermoelectric performance along the crystal growth direction. Unfortunately, poor mechanical stability of zone melted ingots makes it difficult to fabricate devices (especially micro-devices) due to an easy cleavage of the material along the basal plane during manufacturing and assembling of TE modules.[4,5] Therefore, the synthesis of bulk Bi_2Te_3-based materials with simultaneously excellent mechanical and thermoelectric properties has been a focus for the thermoelectric community for some time.

In the past ten years, numerous investigations have shown that carefully chosen nanometer-scale inclusions can scatter phonons very effectively while having a minor impact on the electronic transport, and their presence thus can enhance thermoelectric properties of the material.[6-19] Moreover, the refinement of the grain structure leads to improved mechanical properties of bulk materials according to the Hall–Patch relation.[20] In 2007, Tang et al. reported the maximum *ZT* value of 1.35 at 300 K for the sample prepared by melt spinning with roller linear speed of 40 m s^{-1}.[21] In 2008, Poudel et al. successfully prepared nanostructured p-type Bi_2Te_3-based materials utilizing the ball milling technique followed by hot pressing and obtained the *ZT* value as high as 1.4 at 373

This article is protected by copyright. All rights reserved.

K.[22] Besides, Cao et al. employed a hydrothermal method combined with hot pressing to prepare p-type Bi_2Te_3-based bulk nanocomposites which showed the maximum *ZT* value of 1.47 at approximately 420 K.[23] Furthermore, Xie et al. reported the highest *ZT* of about 1.50 around 300 K for their p-type $(Bi,Sb)_2Te_3$ bulk material synthesized by melt spinning combined with the subsequent spark plasma sintering technique (MS-SPS).[24,25] This material possessed a very fine grain structure due to exceptionally rapid solidification, a typical feature of the melt-spinning process. Moreover, the compressive and bending strength of this material was increased 5-6 times in comparison to ZM ingots.[26] In addition, the MS-SPS synthesis technique has also been used in the preparation of high performance bulk thermoelectric materials, such as skutterudites,[27-29] higher manganese silicides,[30] $AgSbTe_2$,[31] $Mg_2(Si,Sn)$,[32] β-Zn_4Sb_3,[33] and BiSb alloys.[34] Although nanostructured materials with greatly improved thermoelectric and mechanical properties can be obtained by all the above synthesis techniques, the resulting nanocomposite structures have been only small research-size ingots with typical dimensions of 10-15 mm in diameter and 2-3 mm in thickness. Of critical importance for large-scale commercial applications is the synthesis of large-size homogeneous ingots having excellent TE performance and outstanding mechanical properties over the entire length of the samples and doing so consistently and reproducibly.[35] Thus far, very little attention has been focused on reproducibility, homogeneity and consistency of TE properties of large-size nanostructured bulk ingots fabricated by the novel synthesis techniques.

This article is protected by copyright. All rights reserved.

In this work, p-type Bi_2Te_3-based thermoelectric materials were prepared in larger sizes by melt spinning combined with plasma activated sintering. The impact of ingot size and structure of the graphite die on the homogeneity, temperature distribution during the sintering process, and thermoelectric properties are investigated using the finite element analysis aided by Ansys® (Ansys Inc., Cecil Township, PA, USA). Large-size ingots with 30 mm, 40 mm, 60 mm in diameter were successfully prepared and were carefully examined for homogeneity, reproducibility, mechanical properties and TE performance. The study has pointed out a new direction for the synthesis of large-size nanostructured ingots with high repeatability, consistency and uniformity, which is of great relevance for large-scale commercial applications of high performance nanostructured Bi_2Te_3-based thermoelectric materials, especially as it concerns the fabrication of thermoelectric micro-devices.

2. Results and Discussion

Figure 1 shows the distribution of Seebeck coefficient values measured over a cross sectional area of ingots of different size sintered at 723 K with the holding time of 5 min. The measurement interval is 200 μm and the spatial resolution is about 10 μm, as shown in Figure S1. Figure 1(a) depicts the distribution of room temperature values of the Seebeck coefficient obtained on an ingot with the diameter of 15 mm and the thickness of 2 mm. The values of the Seebeck coefficient fall within the range from 200 to 215 $\mu V\ K^{-1}$, roughly within the error bar for the measurement, indicating a uniform distribution for small-size ingots. However, large-size ingots with the diameter

This article is protected by copyright. All rights reserved.

of 30 mm and the thickness of 12 mm have a distinctly inhomogeneous distribution of Seebeck coefficient values varying from 185 to 225 μV K^{-1}, as shown in Figure 1(b) and (c). The Seebeck coefficient on the outer edge of the ingot is larger than the Seebeck coefficient in the center of the ingot. The variation of Seebeck coefficient values resembles an elliptical shape with the Seebeck coefficient decreasing towards the center. As the volume of the ingot increases, the homogeneity of the Seebeck coefficient values becomes progressively worse and this would restrict large scale applications for the MS-PAS synthesized samples.

In order to study the uniformity of large-size ingots more systematically, the electrical conductivity, the Seebeck coefficient and the thermal conductivity were measured at different locations of the ingot along the same direction as shown in **Figures 2**, **3** and **4**. Figure 2 gives the radial and axial distribution of the electrical conductivity for samples cut from the ingot with the diameter of 30 mm and the thickness of 12 mm. The electrical conductivities decrease monotonically with the increasing temperature, behaving like a degenerate semiconductor. Moreover, in the radial direction, the closer the sample comes from the center of the ingot the higher is its electrical conductivity. The room temperature electrical conductivity in the central position is 11.4×10^4 S m^{-1} while the electrical conductivity at the edge of the ingot is 9.6×10^4 S m^{-1} as shown in Figure 2(a). In the axial direction, the electrical conductivity shows the same trend as in the radial direction as shown in Figure 2(b). Specifically, the room temperature electrical conductivity is 9.9×10^4 S m^{-1} in the central position while the electrical conductivity decreases down to 8.1×10^4 S m^{-1} as one goes

This article is protected by copyright. All rights reserved.

toward the top and bottom surfaces of the ingot. An exactly opposite trend is displayed by the Seebeck coefficient in Figure 3 where at the central position the Seebeck coefficient is 190 μV K^{-1} while towards the edge of the ingot the Seebeck coefficient value is higher at 208 μV K^{-1}. ZEM-3 results, which represent averages of the Seebeck coefficient across the sample, are consistent with the scanning Seebeck probe data, indicating that the latter technique is eminently suitable for the characterization of the uniformity of the material.

Similar to the electronic properties, the thermal conductivity too displays certain irregularity in the distribution of its values. As shown in Figure 4, in the radial direction, the room temperature thermal conductivity is about 1.2 W m^{-1} K^{-1} at the center and is higher than the thermal conductivity at the edge (about 1.1 W m^{-1} K^{-1}). However, these changes are quite small and within the error bars of the measurement. In the axial direction, the room temperature thermal conductivity at different locations is almost the same with the value of about 1.3 W m^{-1} K^{-1}. Bulk samples used in measurements of the thermal conductivity were also used to determine the degree of orientation with the Lotgering method shown in **Figure 5**.[36,37] In this method, F is expressed as the following equations: $F=(P-P_0)/(1-P_0)$, $P_0=I_{0(00l)}/\sum I_{0(hkl)}$, $P=I_{(00l)}/\sum I_{(hkl)}$, where $I_{0(00l)}$ is the intensity of (00l) peaks and $\sum I_{0(hkl)}$ is the sum of intensities of all peaks for the powders with random orientation; $I_{(00l)}$ is the (00l) peak intensity and $\sum I_{(hkl)}$ is the sum of the intensities of all peaks for the measured section. The orientation factor of different regions in both the radial and axial direction is on the order of 0.03-0.05, indicating almost no preferential orientation in accord with the negligible change in the

This article is protected by copyright. All rights reserved.

thermal conductivity measured in different directions. Thus the difference in thermoelectric properties between the edge region and the middle is not induced by the difference in preferential orientation.

Numerous investigations have demonstrated that thermoelectric properties have a close relationship with the structure, morphology and composition of the materials. All such factors are closely related to the temperature distribution during the sintering process of large-size ingots. Hence, we used a commercial finite element code, Ansys to simulate the temperature distribution during the sintering process, applying a thermal–electrical coupled steady-state analysis with a very short time of 1 s.[38] Boundary conditions and the load used for the analysis are as follows: (a) the initial temperature during the experiment is 298 K; (b) the temperature of the environment is set as a constant 298 K during the entire process; (c) heat losses by convection are ignored for experiments taking place under vacuum; (d) an electric current I is directly applied at the top surface of the punch, (e) the voltage difference between the top and bottom punches is V; (f) heat transfer by radiation occurs from exposed surfaces of the die, punch, and environment, and we assume the emissivity value of 0.8 which has been confirmed to be very realistic for graphite.[39,40] In order to obtain basic data for the Ansys analysis, we sintered ingots at 373-723 K with no holding time, and their transport properties at the sintering temperature were characterized as shown in Figure S2, S3 and S4. In addition, the basic data for graphite were taken from the literature and the results are shown in **Figure 6** and **7**.[41, 42] The ingot with the diameter of 15 mm and the thickness of 3 mm

This article is protected by copyright. All rights reserved.

shows uniform temperature distribution by the Ansys finite element analysis, and the maximum temperature difference between the center and the edge of the ingot is less than 1 K, as shown in Figure 6. However, the ingot with the diameter of 30 mm and thickness of 12 mm, shown in Figure 7, has the temperature at the center higher than at the edge by as much as 10 K. This, of course, may lead to notable differences in physical and chemical properties of samples depending on from what region of the ingot they were cut out. This is especially important and relevant in regard to the density of anti-site defects and vacancies which are very sensitive to the temperature. The similarity in the ellipsoidal shape distribution of the temperature field and that of the distribution of the Seebeck coefficient values suggests that the cause of these distributions is a particular temperature profile during the sintering process. Since the temperature distribution of the ingots is very difficult to measure. And it is also a challenge to reveal the real temperature through simulation, thus 10 K obtained by simulation is not the real temperature gradient in the ingots during the sintering process. However, the simulation demonstrates the trend of temperature distribution of the ingots during the PAS process. Indeed the temperature gradient in the ingots induced the inhomogeneous distribution of Seebeck coefficient.

In order to further prove that the non-uniform thermoelectric properties of the material are chiefly induced by the inhomogeneous temperature distribution during the sintering process, we have consolidated small size ingots with 15 mm diameter and 2.5 mm thickness at different temperatures from 623 K to 763 K and characterized their thermoelectric properties.[43,44] The aim

This article is protected by copyright. All rights reserved.

here is to explore what effect the sintering temperature has on thermoelectric properties of small-size ingots and, based on the outcome, find remedies and adjust sintering conditions for fabrication of homogeneous large-size ingots.

The small-size ingots sintered at different temperatures are almost isotropic as shown in Figure S5.[45] As shown in Figure S6, the electrical conductivity increases with the increasing sintering temperature except for sample sintered at 743 K and 763 K where an anomalous decrease in the electrical conductivity has occurred. This is due to the fact that the starting material (commercial ZM $Bi_{0.5}Sb_{1.5}Te_3$) contained a slight excess of Te and at the sintering temperatures of 743 K and 763 K the melting point of Te (T_m=722 K) was exceeded and some Te squeezed out of the sample. Indeed, the graphite die after sintering at these temperatures contained droplets of solidified Te. Ingots sintered at 703 K and 723 K achieved the maximum *ZT* value of 1.15, and the detailed thermoelectric performance of ingots sintered at different temperatures is shown in Figures S6-S9. Except for ingots sintered at 743 K and 763 K, the electrical conductivity increases and the Seebeck coefficient decreases with the increasing sintering temperature due to the increasing concentration of charge carriers. **Figure 8** shows the actual composition and carrier concentration of ingots with the diameter of 15 mm and thickness of 2.5 mm at different sintering temperatures between 623 K and 763 K. With the increasing sintering temperature, the ratio of anions to cations decreases and the carrier concentration increases, with the two parameters being closely related.[46,47] For p-type

This article is protected by copyright. All rights reserved.

Bi_2Te_3-based alloys, the carrier concentration is closely related to anti-site defects and vacancies as follows:[48-51]

$$Bi_2Te_3 = 2Bi'_{Te} + 2V_{Bi} + V_{Te} + \frac{3}{2}Te_2 + 2h \quad (1)$$

$$Sb_2Te_3 = 2Sb'_{Te} + 2V_{Sb} + V_{Te} + \frac{3}{2}Te_2 + 2h \quad (2)$$

With the increase in the sintering temperature, a certain amount of Te volatilizes, leading to a decrease in the ratio of anions to cations, and this induces the formation of more anti-site defects resulting in an increase in the density of holes. For large-size ingots, in both the radial and axial directions, the temperature and the hole concentration at the center is higher than at the edge, according to the Ansys finite element analysis, leading to higher electrical conductivity and lower Seebeck coefficient at the center compared with the edge region of the ingot. Variations in the composition of the nominally homogeneous small-size ingots sintered at different temperatures show a similar trend as changes in the charge carrier density at different locations observed in large-size ingots. This makes it plausible that the source of both is the non-uniformity of the temperature field during the synthesis.

In order to improve the uniformity of the temperature field, we have experimented with extending the time during which the ingot is subjected to sintering from 5 min to 30 min. **Figure 9** shows the distribution of Seebeck coefficient values measured over the cross section of large-size

This article is protected by copyright. All rights reserved.

ingots sintered for the time spanning from 5 min to 30 min. As follows from Figure 9, the uniformity of the distribution is greatly improved with the increasing sintering time. Although some differences in the distribution of Seebeck coefficient values (at a level of about 25-30 μV K^{-1} between the center and the edge regions of the ingot) still exist in an ingot sintered for 20 min, the uniformity is much improved compared to an ingot sintered for 5 min. The statistical distribution of Seebeck coefficient is a more understandable way as shown in **Figure 10**. The ingot sintering for 5 min shows average value 197.5 μV K^{-1} and standard deviation 7.6 μV K^{-1} for Seebeck coefficient, while for the ingot sintering for 30 min average value is 187.7 μV K^{-1} and standard deviation is 5.8 μV K^{-1}. With the increase of sinter time, the standard deviation decreases, indicating enhanced homogeneity of Seebeck coefficient which is determined by compositional homogeneity. The effect on transport properties is shown in **Figures 11** and is clear: the variation in the electrical conductivity and the Seebeck coefficient at different locations in both the radial and axial directions of the ingot is much smaller when the time of sintering is extended. Since diffusion, mass transport and thermal transport are time dependent processes, extending the time of sintering allows for achieving a more uniform temperature field which, in turn, results in more uniform transport coefficients.

As already noted, the economy of large-scale industrial applications of thermoelectricity demands a consistent and repeatable fabrication of large-size ingots with good homogeneity and uniformity. In order to ascertain the repeatability and consistency of the material, the identical 20 min sintering process was used to prepare two ingots with the diameter of 30 mm and the height of

This article is protected by copyright. All rights reserved.

12 mm and the distribution of Seebeck coefficient values was measured over the cross section by the scanning Seebeck probe. As shown in **Figure 12**, the two ingots have almost the same distribution of Seebeck coefficient values confirming that the MS-PAS synthesis route has excellent repeatability and consistence which is so essential for the fabrication of large-size ingots of thermoelectric materials. One simply has to find, by the trial and error, the appropriate sintering conditions which, in the case of Bi_2Te_3-based materials, seem to require an extended duration of sintering.

It is noted that the inhomogeneous distribution of Seebeck of MS-PAS ingot is ascribed to compositional variation of the ratio between anions and cations, induced by temperature gradient in the ingot. However the temperature gradient in the ingots is strongly related to the inhomogeneous joule heat and heat transfer during PAS process which can be correlated to the structure of graphite die. Therefore, the uniformity of the temperature distribution in the ingots can be improved through appreciate design of the graphite die. Here we choose the die with the inner diameter 30 mm as an example with variation of the outer diameter from 60 mm to 120 mm. **Figure 13** shows the temperature of ingot (30 mm diameter and 12 mm height) along radial and axial direction obtained by Ansys simulation sintering at 723 K by graphite die with different outer diameter. With increase of the outer diameter of graphite die, the temperature gradient increases along both radial and axial direction. And the further experimental results confirm that the simulation is justified as shown in **Figure 14**. The standard deviation of Seebeck coefficient over the cross section of ingot sintered for 5

This article is protected by copyright. All rights reserved.

min with graphite die 60 mm in outer diameter is 6.3 μV K^{-1} according to statistical distribution, much smaller than that of ingots sintered with graphite die 90 mm and 120 mm in outer diameter. As a result, the homogeneity of ingot (30 mm diameter and 12 mm height) is improved by appreciate designing of the graphite die.

In **Figure 15** we compare the dimensionless thermoelectric figure of merit *ZT* of two samples cut out from a large-size (30 mm diameter and 12 mm height) ingot parallel and perpendicular to the ingot's axis prepared by the MS-PAS techniques (20 min sintering time) with the figure of merit measured for a ZM sample and for two samples prepared by the traditional melting followed by spark plasma sintering, M-SPS, (again, samples cut out parallel and perpendicular to the ingot's axis). *ZT* values of the two samples cut out from the MS-PAS ingot are almost the same and the maximum value of 1.15 is achieved at 373 K. This represents about 17% enhancement compared to the ZM sample where the *ZT* peaks at a value of 0.98 at temperatures closer to the ambient.[26] The two M-SPS samples cut out from the 30 mm diameter ingot reach the maximum value of *ZT* of about unity at about 380 K.[52]

Moreover, larger ingots with 40 mm and 60 mm in diameter were synthesized by MS-PAS. **Figure 16** shows the distribution of Seebeck coefficient values over the cross section of ingots with diameter 40 mm and 60 mm respectively. For comparison, the data of Zone melting ingots is also shown in Figure 16. With increase of the ingot diameter, indeed the homogeneity of the ingots deteriorate. **Figure 17** shows the statistical distributions of the Seebeck coefficient values over the

This article is protected by copyright. All rights reserved.

cross section of ingots for ingots with diameter 40 mm, 60 mm and Zone melting ingots respectively. The Seebeck coefficient of ingot with 40 mm in diameter posseses average value 189.5 μV K^{-1} and standard deviation 7.2 μV K^{-1}. Those for the ingot with 60 mm in diameter are 205.8 μV K^{-1}, 8.7 μV K^{-1} for average value and standard deviation respectively. While the ZM sample exhibits average value 217.3 μV K^{-1} and standard deviation 10.9 μV K^{-1}. Clearly, the standard deviation of MS-PAS ingots is smaller than that of Zone melting samples in spite of that Zone melting process is an equilibrium process, indicating that the uniformity of the Seebeck coefficient values in the MS-PAS ingot is far better than that of the ZM ingot.

Advantages of the MS-PAS synthesized ingots over the ZM ingot, as far as the compressive strength and the bending strength is concerned, are documented by the data in **Figure 18** where a data point constitutes an average value of 10 samples. The compressive and the bending strengths of the ZM sample are similar, with a value of 10 MPa. A sample cut from a large-size ingot prepared by MS-PAS with the sintering time of 5 min has the compressive strength of 56 MPa and the bending strength of 27 MPa. These values increase with the time of sintering and a sample cut from a large-size ingot sintered for 20 min reaches 65 MPa in the compressive strength and 40 MPa in the bending strength, values considerably higher than for the ingot sintered for 5 min and some 3-5 times greater strengths than for the ZM sample. The improvement comes from a diminishing presence of the Te boundary phase upon increasing the time of sintering as documented by the BSE image in Figure S10. This is further confirmed by TEM studies shown in **Figure 19**. Images for a

This article is protected by copyright. All rights reserved.

sample from the MS-PAS prepared ingot sintered for 5 min are shown in Figures 19(a-d). Grains 1 and 3 in Figure 19(a) are the matrix phase confirmed by SAED and EDS in Figures 19(b-d). Moreover, EDS in Figure 19(d) also shows that the interfacial phase (grain 2 in Figure 19(a)) is, indeed, the Te phase of micrometer scale. HRTEM image of a sample from the MS-PAS prepared ingot sintered for 20 min, Figure 19(e), shows convincingly that the amount of interfacial Te is dramatically reduced and the width of the interfacial phase region shrinks down to 10 nm. The much narrowed interface region renders a more compact structure with improved mechanical properties.

3. Conclusion

In this study, the effect of temperature distribution during the process of sintering of Bi_2Te_3-based thermoelectric materials on their thermoelectric properties is discussed in depth. Large-size ingots show higher temperature and larger carrier concentration at locations near the axis of the ingots than at locations close to the edges of the ingots. Although some temperature difference during the sintering process is inevitable, the uniformity of sintered ingots are greatly improved by extending the duration of sintering and design of graphite die. Large-size ingots sintered for 20 min attain the maximum *ZT* value of 1.15 at 373 K and exhibit the compressive strength of 65 MPa and the bending strength of 40 MPa. These large-size ingots are prepared by melt spinning (MS) followed by plasma activated sintering (PAS) and show enhanced thermoelectric properties, much better mechanical properties and improved homogeneity compared to the ZM prepared ingots. This bodes

This article is protected by copyright. All rights reserved.

well for economical fabrication of commercial quantities of high performance TE materials intended for applications in both TE cooling and power generation.

4. Experimental Section

Commercially available p-type $Bi_{0.5}Sb_{1.5}Te_3$ ZM ingots (Thermonamic Electronics Corporation) were used as starting materials for the melt-spinning process. The ZM ingots were put into a quartz tube with a 0.5 mm diameter nozzle, and placed under the protection of an argon atmosphere. The ingots of about 15 gram were melted by induction melting and then ejected under an argon atmosphere with a pressure of 0.04 MPa in about 20 s onto a copper roller rotating with the linear speed of 10 m s^{-1}. Figure S11 shows the morphology of obtained thin ribbons. Enough ribbon products were obtained by repeated melting and ejection, and the ribbons were subsequently hand-grounded into fine powders. Large-size samples with 30 mm, 40 mm, 60 mm diameter were sintered at 723 K under the pressure of 30 MPa for different time duration in the vacuum by the plasma activated sintering (PAS) technique, similar to SPS. [53] Figure S12 shows the image of an ingot with 30 mm diameter and 12 mm height after sintering, and Figure 16(c) and Figure 16(d) show the image of ingots with 40 mm and 60 mm in diameter respectively. In addition, in order to investigate the impact of the sintering temperature on thermoelectric properties, smaller-size ingots of 15 mm in diameter and 2-3 mm in height were sintered at different sintering temperatures (623-763 K).

This article is protected by copyright. All rights reserved.

Phase identification of the ingots was performed by powder X-ray diffraction with Cu Kα radiation (XRD, PANalytical Empyrean, Netherlands), the diffractometer was operated at 40 kV and 40 mA. The actual composition was obtained by electron-probe microanalysis (EPMA, JXA-8230, JEOL, Japan). Microstructures of the ingots were investigated by field-emission scanning electron microscopy (FESEM, Hitachi SU-8020, Japan), and high-resolution transmission electron microscopy (HRTEM, JEM-2100F, JEOL, Japan).

The electrical conductivity (σ) and the Seebeck coefficient (α) were measured simultaneously using commercial equipment (ZEM-3, Ulvac Riko, Inc.) under a low pressure of inert gas (He) in the range of 298–523 K. The thermal conductivity (κ) was calculated from the relationship $\kappa = DC_p d$, where D is the thermal diffusivity obtained by the laser flash method (LFA-457, Netzsch, German), C_p is the specific heat measured by a differential scanning calorimeter (DSC Q20, TA Instrument, USA), and d is the density measured by the Archimedes method. The Hall coefficient (R_H) at room temperature was determined by a physical properties measurements system (PPMS-9, Quantum Design, USA) with the magnetic field of 1 T. The corresponding carrier concentration (n) and carrier mobility (μ_H) were calculated by the following equations: $n = 1/eR_H$ and $\mu_H = \sigma/ne$. The variation of the Seebeck coefficient over the cross section was characterized by a Scanning Seebeck Microprobe (Panco, Germany).[54-57] The compressive and bending strengths were measured on a MTS universal test machine (E44.104, MTS, China). The size of the measured samples was 6 × 3 × 3 mm^3 for the

This article is protected by copyright. All rights reserved.

compressive strength and 15 × 2 × 2 mm^3 for the bending strength. The average of 10 samples was used to evaluate the compressive and bending strengths.

Supporting Information

Supporting Information is available from the Wiley Online Library or from the author.

Acknowledgements

The authors thank Rong Jiang and Tingting Luo for help with the HRTEM analysis. The authors wish to acknowledge support from the National Basic Research Program of China (973 program) under project 2013CB632502, the International Science & Technology Cooperation Program of China (Grant No. 2011DFB60150), the Natural Science Foundation of China (Grant No. 51402222, 51172174, 51521001) and the 111 Project of China(Grant No. B07040). C. U. and X. T. also acknowledge support provided by CERC-CVC under the Award Number DE-PI0000012. At Northwestern MGK is supported by the Department of Energy, Office of Science Basic Energy Sciences grant DE-SC0014520.

Received: ((will be filled in by the editorial staff))
Revised: ((will be filled in by the editorial staff))
Published online: ((will be filled in by the editorial staff))

[1] L. E. Bell, *Science* **2008**, 321, 1457.

[2] G. J. Snyder, E. S. Toberer, *Nat. Mater*. **2008**, 7, 105.

[3] T. C. Harman, P. J. Taylor, M. P. Walsh, B. E. LaForge, *Science* **2002**, 297, 2229.

This article is protected by copyright. All rights reserved.

[4] J. Jiang, L. D. Chen, S. Q. Bai, Q. Yao, Q. Wang, *J. Cryst. Growth* **2005**, 277, 258.

[5] Y. Zheng, H. Y. Xie, S. C. Shu, Y. G. Yan, H. Li, X. F. Tang, *J. Electron. Mater.* **2013**, 43, 2017.

[6] C. J. Vineis, A. Shakouri, A. Majumdar, M. G. Kanatzidis, *Adv. Mater.* **2010**, 22, 3970.

[7] J. R. Sootsman, D. Y. Chung, M. G. Kanatzidis, *Angew. Chem. Int. Ed.* **2009**, 48, 8616.

[8] M. G. Kanatzidis, *Chem. Mater.* **2010**, 22, 648.

[9] M. S. Dresselhaus, G. Chen, M. Y. Tang, R. G. Yang, H. Lee, D. Z. Wang, Z. F. Ren, J. P. Fleurial, P. Gogna, *Adv. Mater.* **2007**, 19, 1043.

[10] L. P. Hu, H. J. Wu, T. J. Zhu, C. G. Fu, J. Q. He, P. J. Ying, X. B. Zhao, *Adv. Energy Mater.* **2015**, 5, 1500411.

[11] X. L. Su, H. Li, G. Y. Wang, H. Chi, X. Y. Zhou, X. F. Tang, Q. J. Zhang, C. Uher, *Chem. Mater* **2011**, 23, 2948.

[12] Y. C. Lan, A. J. Minnich, G. Chen, Z. F. Ren, *Adv. Funct. Mater.* **2010**, 20, 357.

[13] J. H. Li, Q. Tan, J. F. Li, D. W. Liu, F. Li, Z. Y. Li, M. M. Zou, K. Wang, *Adv. Funct. Mater.* **2013**, 23, 4317.

[14] S. P. Feng, Y. H. Chang, J. Yang, B. Poudel, B. Yu, Z. F. Ren, G. Chen, *Phys. Chem. Chem. Phys.* **2013**, 15, 6757.

This article is protected by copyright. All rights reserved.

[15] Q. H. Zhang, X. Ai, L. J. Wang, Y. X. Chang, W. Luo, W. Jiang, L. D. Chen, *Adv. Funct. Mater.* **2015**, 25, 966.

[16] H. Y. Lv, H. J. Liu, J. Shi, X. F. Tang, C. Uher, *J. Mater. Chem. A* **2013**, 1, 6831.

[17] S. Y. Wang, W. J. Xie, H. Li, X. F. Tang, *Intermetallics* **2011**, 19, 1024.

[18] Y. C. Zhang, T. Day, M. L. Snedaker, H. Wang, S. Kramer, C. S. Birkel, X. L. Ji, D. Y. Liu, G. J. Snyder, G. D. Stucky, *Adv. Mater.* **2012**, 24, 5065.

[19] T. J. Zhu, Z. J. Xu, J. He, J. J. Shen, S. Zhu, L. P. Hu, T. M. Tritt, X. B. Zhao, *J. Mater. Chem. A* **2013**, 1, 11589.

[20] C. E. Carlton, P. J. Ferreira, *Acta Mater.* **2007**, 55, 3749.

[21] X. F. Tang, W. J. Xie, H. Li, W. Y. Zhao, Q. J. Zhang, M. Niino, *Appl. Phys. Lett.* **2007**, 90, 012102.

[22] B. Poudel, Q. Hao, Y. Ma, Y. C. Lan, A. Minnich, B. Yu, X. Yan, D. Z. Wang, A. Muto, D. Vashaee, X.Y. Chen, J. M. Liu, M. S. Dresselhaus, G. Chen, Z. F. Ren, *Science* **2008**, 320, 634.

[23] Y. Q. Cao, X. B. Zhao, T. J. Zhu, X. B. Zhang, J. P. Tu, *Appl. Phys. Lett.* **2008**, 92, 143106.

[24] W. J. Xie, J. He, H. J. Kang, X. F. Tang, S. Zhu, M. Laver, S. Y. Wang, J. R. D. Copley, C. M. Brown, Q. J. Zhang, T. M. Tritt, *Nano lett.* **2010**, 10, 3283.

This article is protected by copyright. All rights reserved.

[25] W. J. Xie, X. F. Tang, Y. G. Yan, Q. J. Zhang, T. M. Tritt, *Appl. Phys. Lett.* **2009**, 94, 102111.

[26] Y. Zheng, Q. Zhang, X. L. Su, H. Y. Xie, S. C. Shu, T. L. Chen, G. J. Tan, Y. G. Yan, X. F. Tang, C. Uher, G. J. Snyder, *Adv. Energy Mater.* **2014**, 5, 1401391.

[27] H. Li, X. F. Tang, Q. J. Zhang, C. Uher, *Appl. Phys. Lett.* **2008**, 93, 252109.

[28] X. L. Su, H. Li, Y. G. Yan, G. Y. Wang, H. Chi, X. Y. Zhou, X. F. Tang, Q. J. Zhang, C. Uher, *Acta Mater.* **2012**, 60, 3536.

[29] G. J. Tan, W. Liu, S. Y. Wang, Y. G. Yan, H. Li, X. F. Tang, C. Uher, *J. Mater. Chem. A* **2013**, 1, 12657.

[30] W. H. Luo, H. Li, Y. G. Yan, Z. B. Lin, X. F. Tang, Q. J. Zhang, C. Uher, *Intermetallics* **2011**, 19, 404.

[31] B. L. Du, H. Li, J. J. Xu, X. F. Tang, C. Uher, *J. Solid State Chem.* **2011**, 184, 109.

[32] Q. Zhang, Y. Zheng, X. L. Su, K. Yin, X. F. Tang, C. Uher, *Scripta Mater.* **2015**, 96, 1.

[33] S. Y. Wang, H. Li, D. K. Qi, W. J. Xie, X. F. Tang, *Acta Mater.* **2011**, 59, 4805.

[34] T. T. Luo, S. Y. Wang, H. Li, X. F. Tang, *Intermetallics* **2013**, 32, 96.

[35] T. B. Holland, U. Anselmi-Tamburini, A. K. Mukherjee, *Scripta Mater.* **2013**, 69, 117.

[36] F. K. Lotgering, *J. Inorg. Nucl. Chem.* **1959**, 9, 113.

This article is protected by copyright. All rights reserved.

[37] G. Zheng, X. L. Su, T. Liang, Q. B. Lu, Y. G. Yan, C. Uher, X. F. Tang, *J. Mater. Chem. A* **2015**, 3, 6603.

[38] F. Chen, S. Yang, J. Y. Wu, J. A. Galaviz Perez, Q. Shen, J. M. Schoenung, E. J. Lavernia, L. M. Zhang, *J. Am. Ceram. Soc.* **2015**, 98, 732.

[39] E. A. Olevsky, C. Garcia-Cardona, W. L. Bradbury, C. D. Haines, D. G. Martin, D. Kapoor, *J. Am. Ceram. Soc.* **2012**, 95, 2414.

[40] K. Vanmeensel, A. Laptev, J. Hennicke, J. Vleugels, O. Vanderbiest, *Acta Mater.* **2005**, 53, 4379.

[41] U. Anselmi-Tamburini, S. Gennari, J. E. Garay, Z. A. Munir, *Mater. Sci. Eng. A* **2005**, 394, 139.

[42] S. Muñoz, U. Anselmi-Tamburini, *J. Mater. Sci.* **2010**, 45, 6528.

[43] X. A. Fan, J. Y. Yang, R. G. Chen, H. S. Yun, W. Zhu, S. Q. Bao, X. K. Duan, *J. Phys. D Appl. Phys.* **2006**, 39, 740.

[44] N. Keawprak, Z. M. Sun, H. Hashimoto, M. W. Barsoum, *J. Alloy Compd.* **2005**, 397, 236.

[45] W. J. Xie, J. He, S. Zhu, T. Holgate, S. Y. Wang, X. F. Tang, Q. J. Zhang, T. M. Tritt, *J. Mater. Res.* **2011**, 26, 1791.

[46] L. P. Hu, T. J. Zhu, X. H. Liu, X. B. Zhao, *Adv. Fun. Mater.* **2014**, 24, 5211.

This article is protected by copyright. All rights reserved.

[47] L. P. Hu, T. J. Zhu, Y. G. Wang, H. H. Xie, Z. J. Xu and X. B. Zhao, *NPG Asia Mater.* **2014**, 6, 88.

[48] T. Thonhauser, G. S. Jeon, G. D. Mahan, J. O. Sofo, *Phys. Rev. B* **2003**, 68, 205207.

[49] J. Jiang, L. D. Chen, S. Q. Bai, Q. Yao, *J. Alloy Compd.* **2005**, 390, 208.

[50] J. Jiang, L. D. Chen, S. Q. Bai, Q. Yao, Q. Wang, *Scripta Mater.* **2005**, 52, 347.

[51] L. D. Zhao, B. P. Zhang, W. S. Liu, H. L. Zhang, J. F. Li, *J. Alloy Compd.* **2009**, 467, 91.

[52] J. J. Shen, L. P. Hu, T. J. Zhu and X. B. Zhao, *Appl. Phys. Lett.* **2011**, 99, 124102.

[53] K. Yamazaki, S.H. Risbud, H. Aoyama, K. Shoda, *J. Mater. Process. Tech.* **1996**, 56, 955.

[54] D. Platzek, G. Karpinski, C. Stiewe, P. Ziolkowski, C. Drasar, E. Müller, in: *Proc. 24th Int. Conf. on Thermoelectrics*, Clemson, USA, 2005, pp. 13-16.

[55] H. Yin, A. B. Blichfeld, M. Christensen, B. B. Iversen, *ACS Appl. Mater. Inter.* **2014**, 6, 10542.

[56] M. Søndergaard, M. Christensen, K. A. Borup, H. Yin, B. B. Iversen, *Acta Mater.* **2012**, 60, 5745.

[57] E. M. J. Hedegaard, S. Johnsen, L. Bjerg, K. A. Borup, B. B. Iversen, *Chem. Mater.* **2014**, 26, 4992.

This article is protected by copyright. All rights reserved.

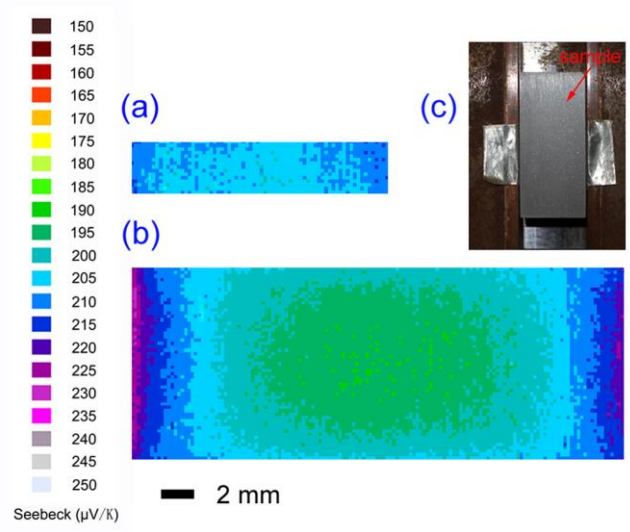

Figure 1. (a) Distribution of Seebeck coefficient values over the cross section of an ingot with the diameter of 15 mm and height of 3 mm; (b) Distribution of Seebeck coefficient values over the cross section of an ingot with the diameter of 30 mm and height 12 mm; (c) an image of the cross section of an ingot with the diameter of 30 mm and height of 12 mm on which the Seebeck coefficient values were measured.

This article is protected by copyright. All rights reserved.

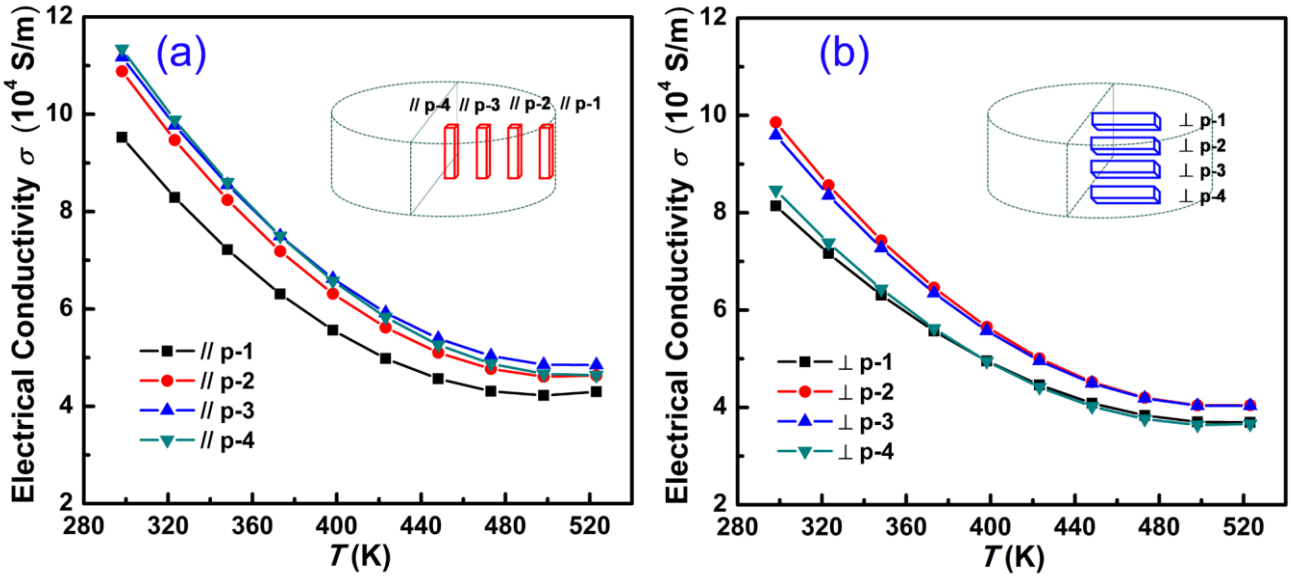

Figure 2. (a) The radial distribution of the electrical conductivity measured on samples cut from the ingot of 30 mm diameter and height of 12 mm and labeled as in the inset of Figure 2(a); (b) the axial distribution of the electrical conductivity measured on samples cut from the ingot of 30 mm diameter and height of 12 mm and labeled as in the inset of Figure 2(b).

This article is protected by copyright. All rights reserved.

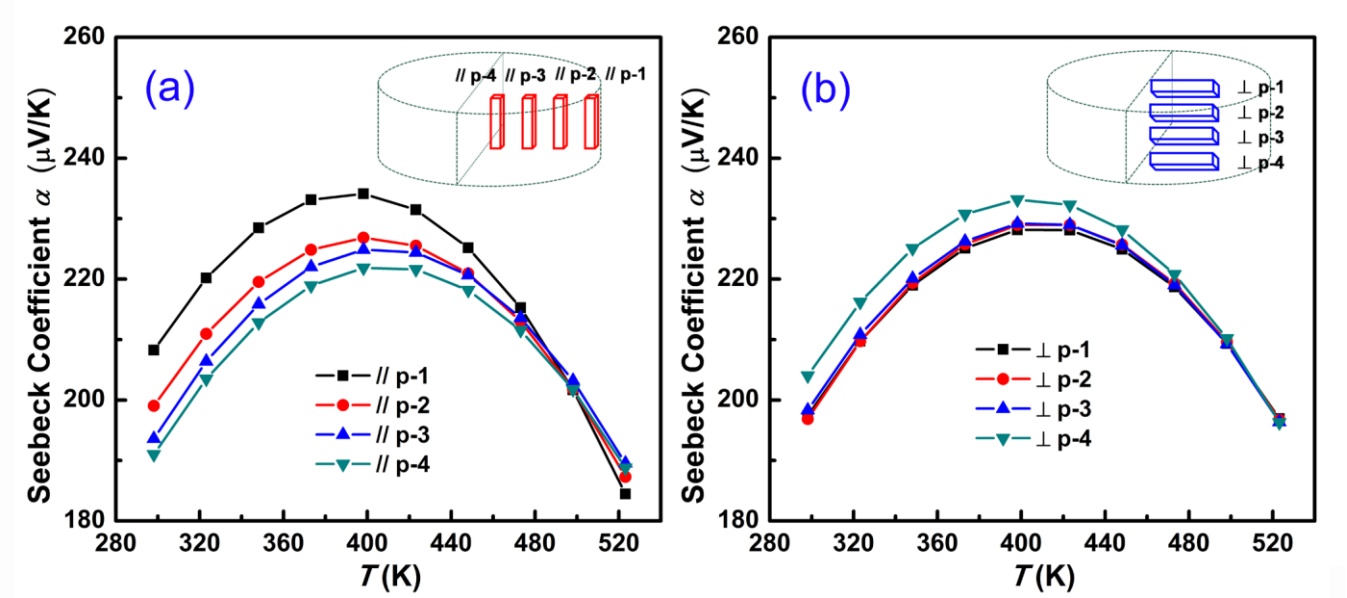

Figure 3. (a) The radial distribution of the Seebeck coefficient measured on samples cut from the ingot with the diameter of 30 mm and height of 12 mm as shown in the inset of Figure 3(a); (b) the axial distribution of the Seebeck coefficient measured on samples cut from the ingot with the diameter of 30 mm and height of 12 mm as shown in the inset of Figure 3(b).

This article is protected by copyright. All rights reserved.

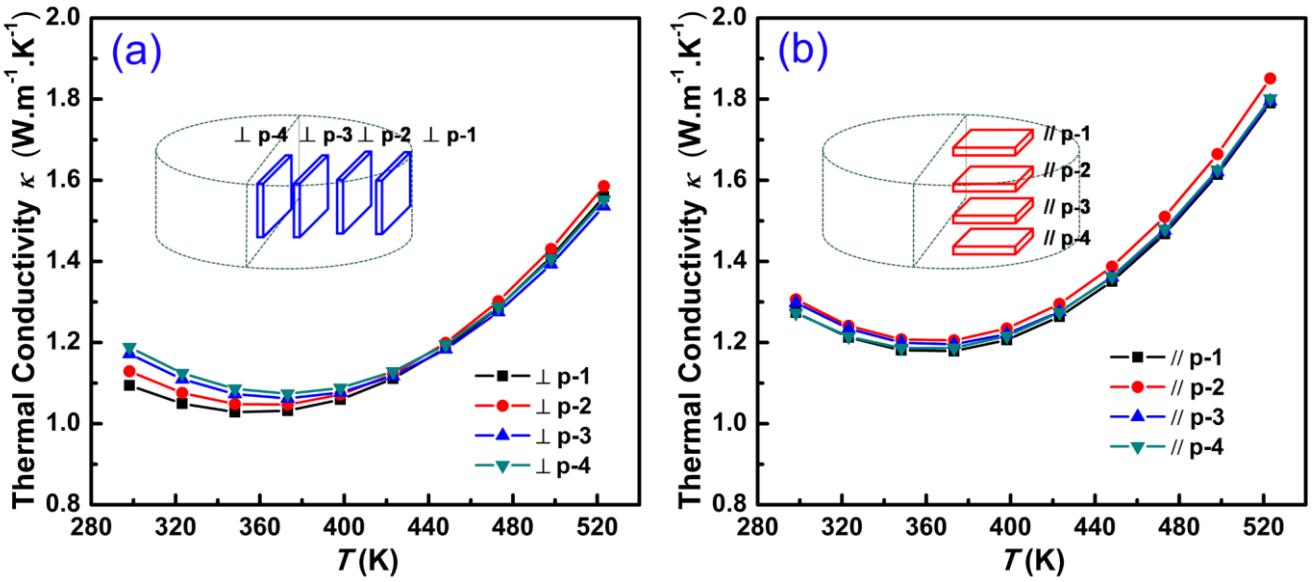

Figure 4. (a) The radial distribution of the thermal conductivity measured on samples cut from the ingot with the diameter of 30 mm and height of 12 mm as shown in the inset of Figure 4(a); (b) the axial distribution of the thermal conductivity measured on samples cut from the ingot with the diameter of 30 mm and height of 12 mm as shown in the inset of Figure 4(b).

This article is protected by copyright. All rights reserved.

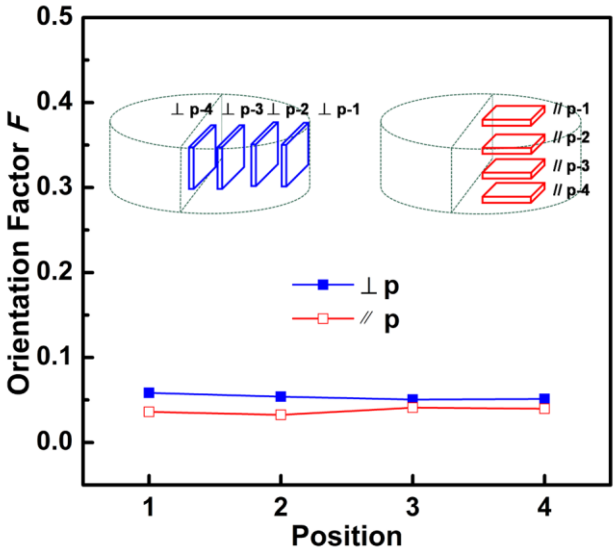

Figure 5. The orientation factor for samples cut from the ingot with the diameter of 30 mm and height 12 mm as indicated in the insets.

This article is protected by copyright. All rights reserved.

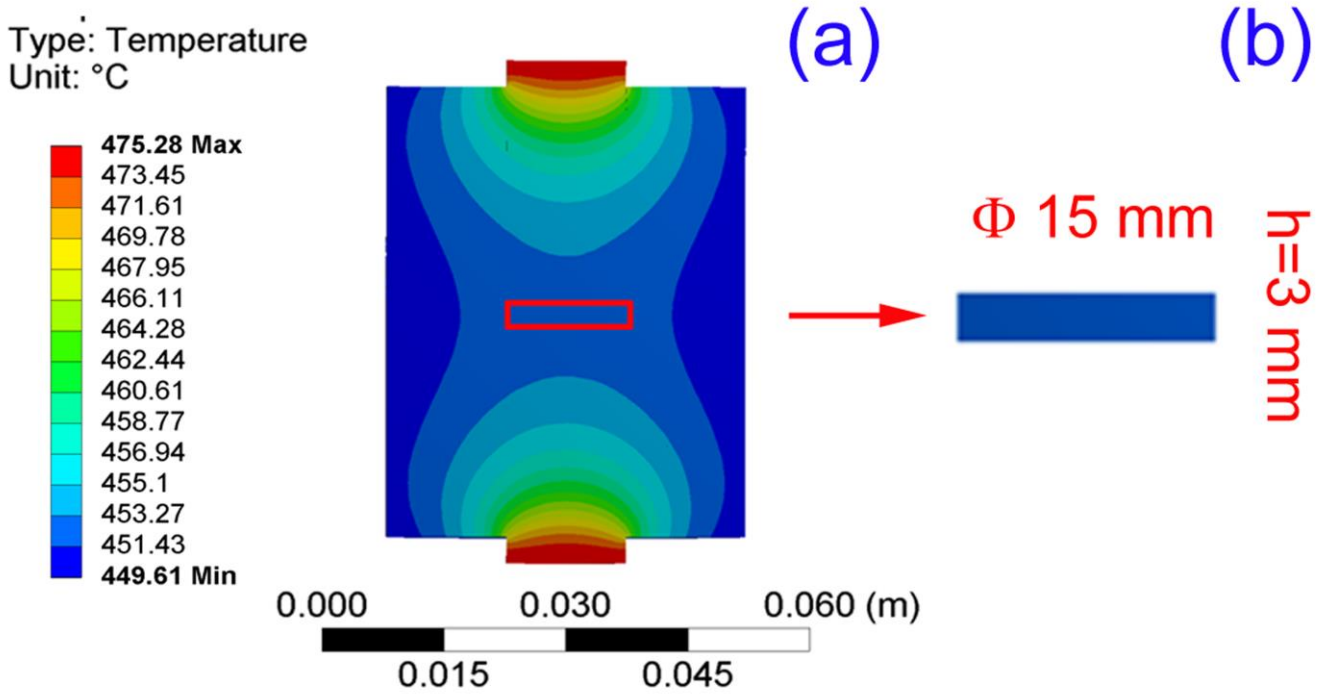

Figure 6. (a) The temperature distribution during sintering for graphite mould and the ingot with the diameter of 15 mm and height of 3 mm; (b) the temperature distribution during sintering for the ingot with the diameter of 15 mm and height of 3 mm.

This article is protected by copyright. All rights reserved.

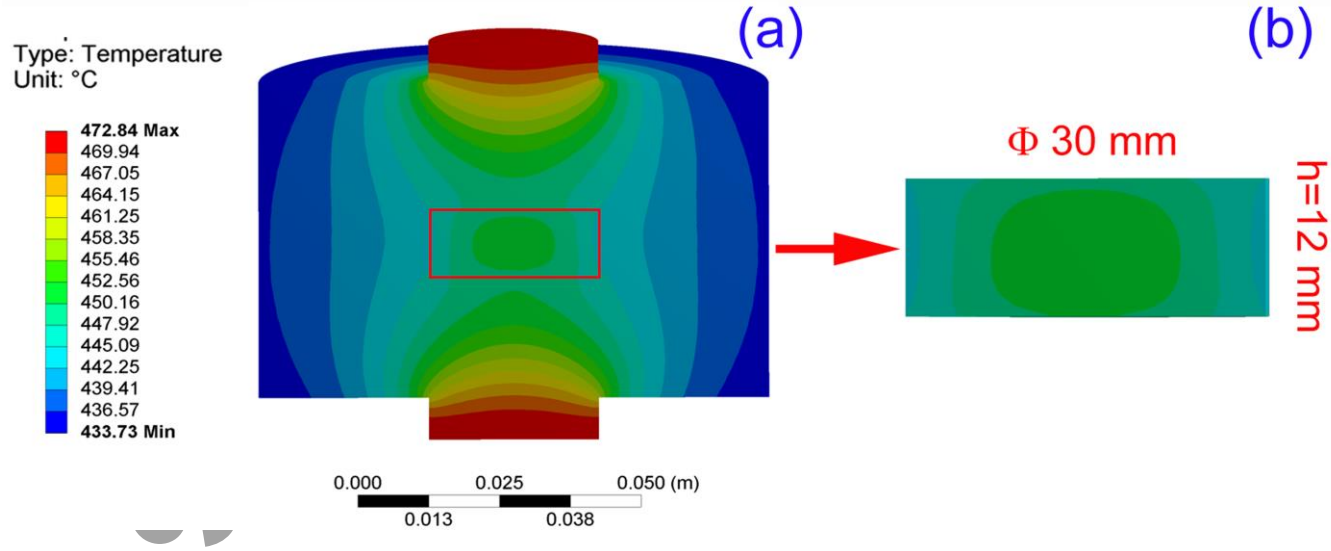

Figure 7. (a) The temperature distribution during sintering for graphite mould and the ingot with the diameter of 30 mm and height of 12 mm; (b) the temperature distribution during sintering for the ingot with the diameter of 30 mm and height of 12 mm.

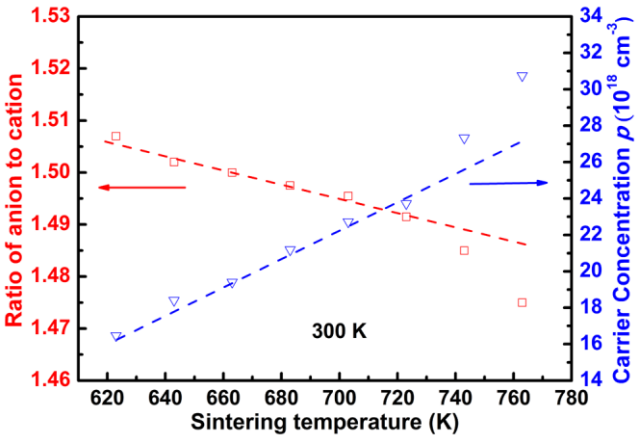

Figure 8. The constituency ratio and the carrier concentration for ingots with the diameter of 15 mm and height of 3 mm sintered at different temperatures between 623 K and 763 K.

This article is protected by copyright. All rights reserved.

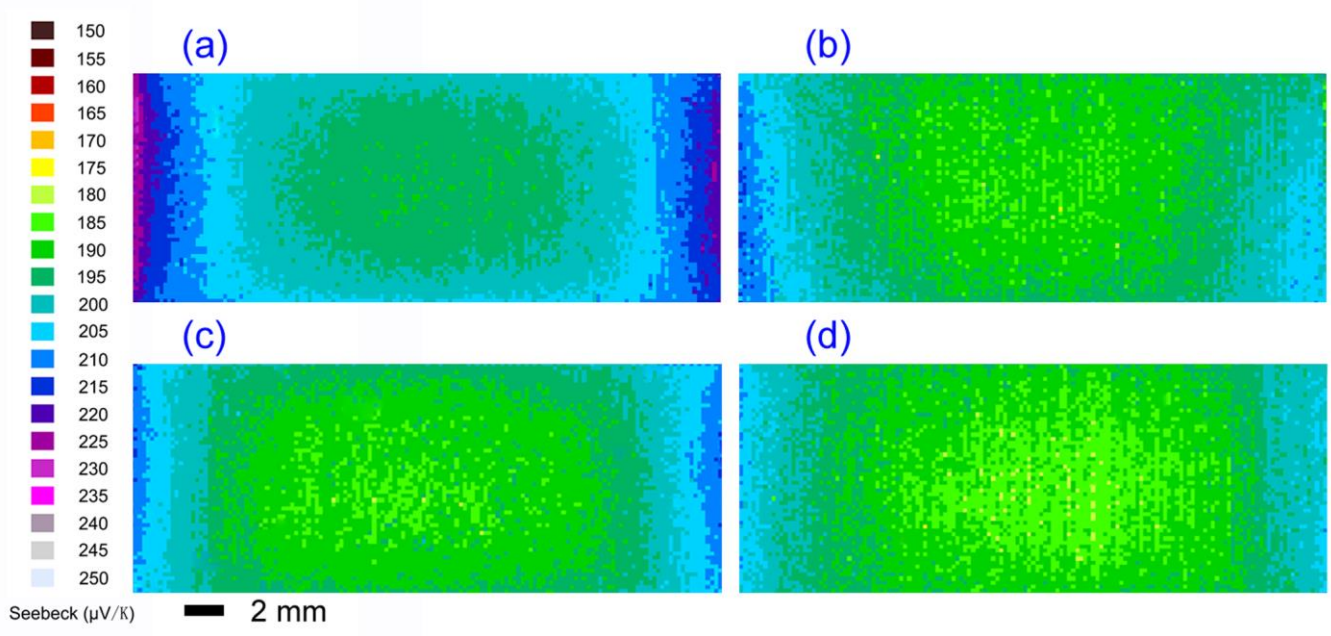

Figure 9. The distribution of Seebeck coefficient values over the cross section of ingots with the diameter of 30 mm and height of 12 mm sintered for the time of (a) 5 min; (b) 10 min; (c) 20 min; and (d) 30 min.

This article is protected by copyright. All rights reserved.

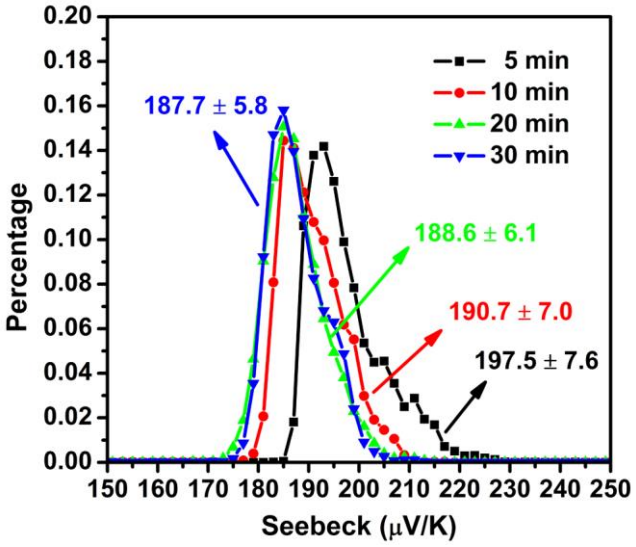

Figure 10. The statistical distribution of Seebeck coefficient for ingots with the diameter of 30 mm and height of 12 mm, and the sintering time is 5 min, 10 min, 20 min and 30 min respectively.

This article is protected by copyright. All rights reserved.

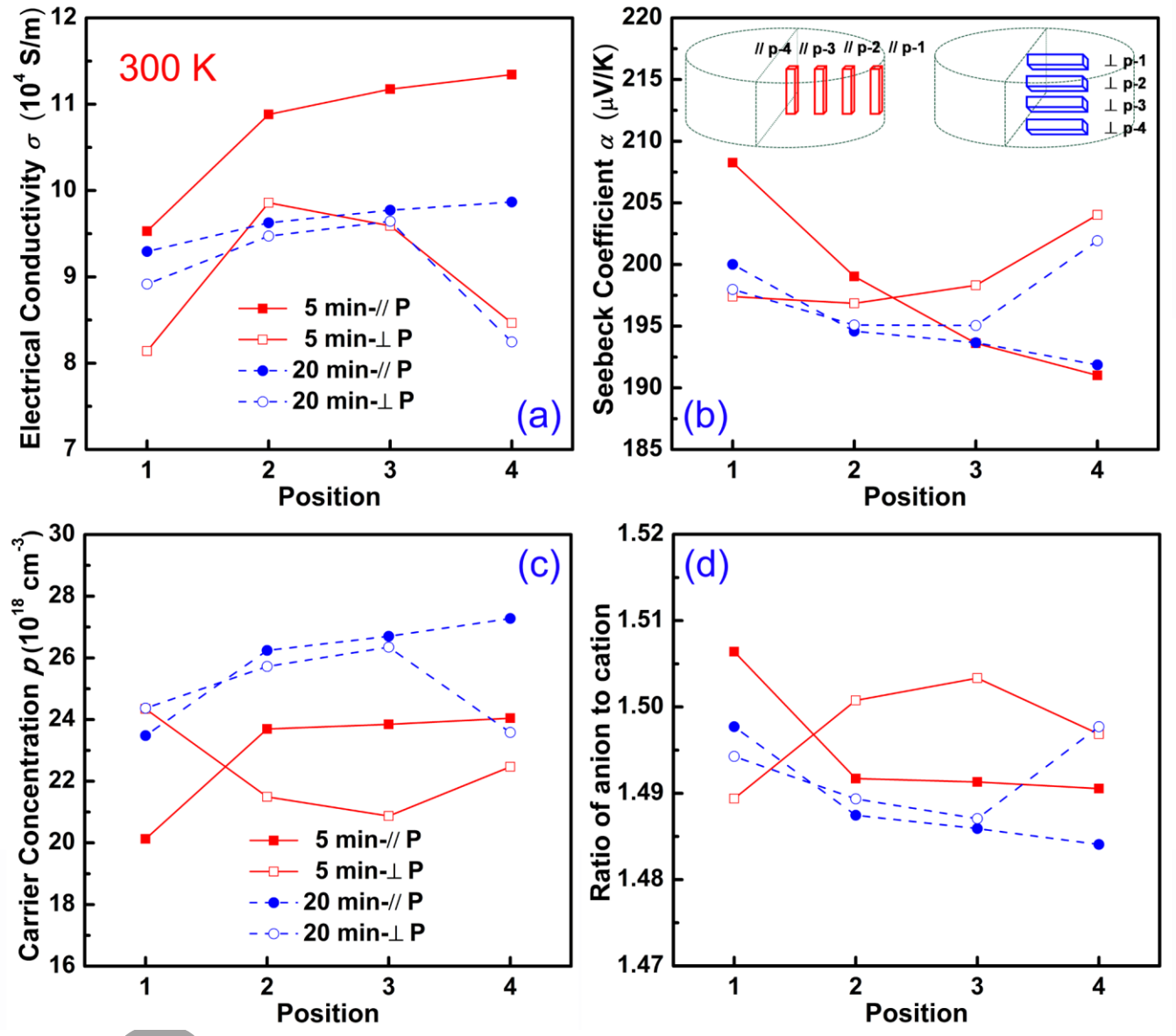

Figure 11. The comparison of transport parameters of samples cut from ingots with the diameter of 30 mm and height of 12 mm and sintered for the time of 5 min and 20 min. (a) electrical conductivity; (b) Seebeck coefficient; (c) carrier concentration; (d) sample composition.

This article is protected by copyright. All rights reserved.

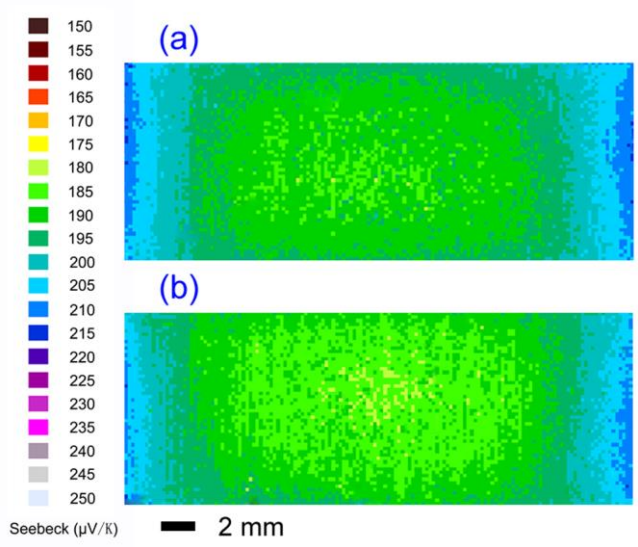

Figure 12. The distribution of Seebeck coefficient values measured over the cross section of two ingots with the diameter of 30 mm and height of 12 mm synthesized under identical conditions and sintered for 20 min. (a) The first sample; (b) the second sample. Excellence reproducibility is apparent.

This article is protected by copyright. All rights reserved.

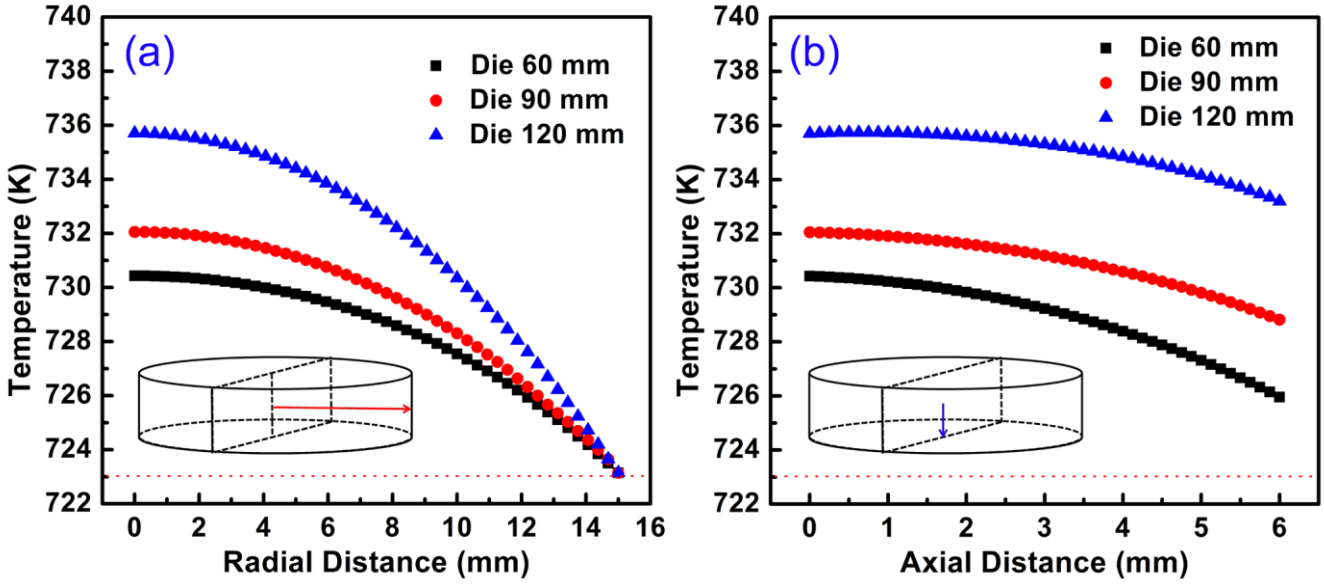

Figure 13. The temperature distribution of ingots sintered by graphite die with different outer diameter. (a) Along radial direction; (b) along axial direction.

This article is protected by copyright. All rights reserved.

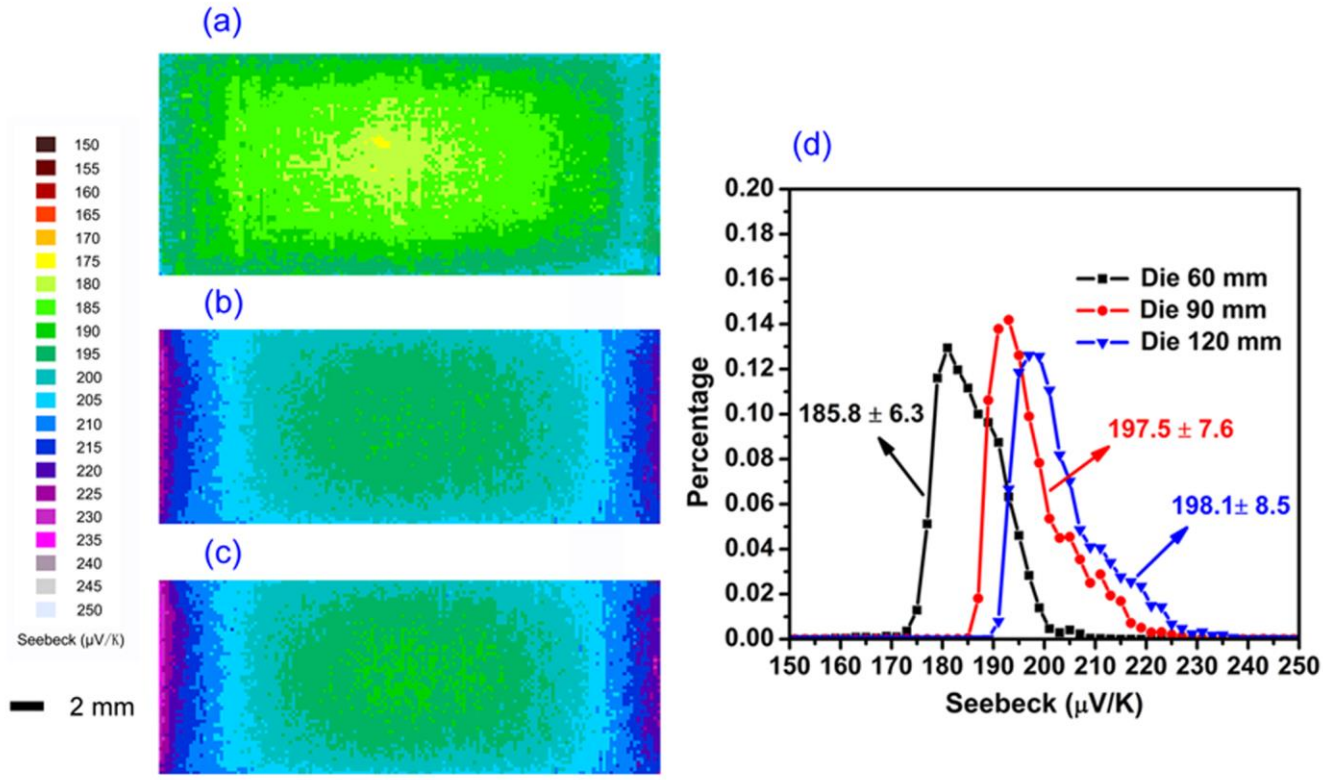

Figure 14. (a) The distribution of Seebeck coefficient values over the cross section of ingots with the diameter of 30 mm and height of 12 mm sintered by graphite die with 60 mm in outer diameter; (b) the distribution of Seebeck coefficient values over the cross section of ingots with the diameter of 30 mm and height of 12 mm sintered by graphite die with 90 mm in outer diameter; (c) the distribution of Seebeck coefficient values over the cross section of ingots with the diameter of 30 mm and height of 12 mm sintered by graphite die with 120 mm in outer diameter; (d) the statistical distribution of Seebeck coefficient for ingots with the diameter of 30 mm and height of 12 mm, and the outer diameter of graphite die is 60 mm, 90 mm, and 120 mm respectively.

This article is protected by copyright. All rights reserved.

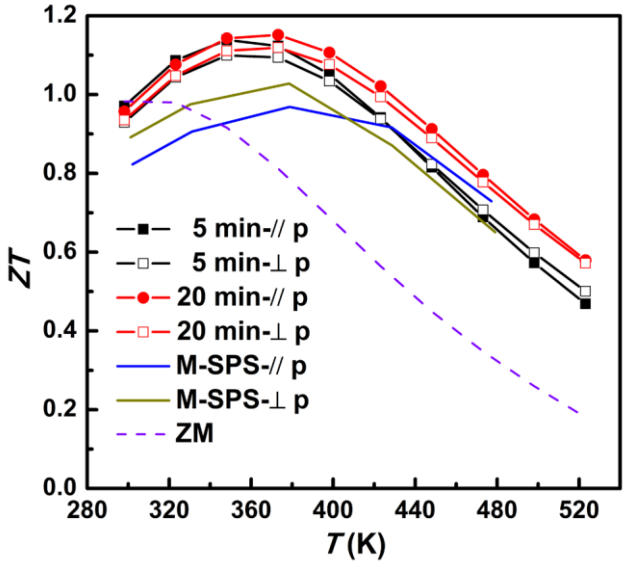

Figure 15. A comparison of *ZT* values measured on different samples. Red solid circles and open squares represent *ZT* values measured parallel and perpendicular to the pressing direction for samples cut from the ingot with the diameter of 30 mm and height of 12 mm and sintered for 20 min. Blue and green curves indicate *ZT* values for samples cut parallel and perpendicular to the pressing direction from the ingot prepared by melting followed by SPS. The dashed line stands for *ZT* values measured on a ZM sample.

This article is protected by copyright. All rights reserved.

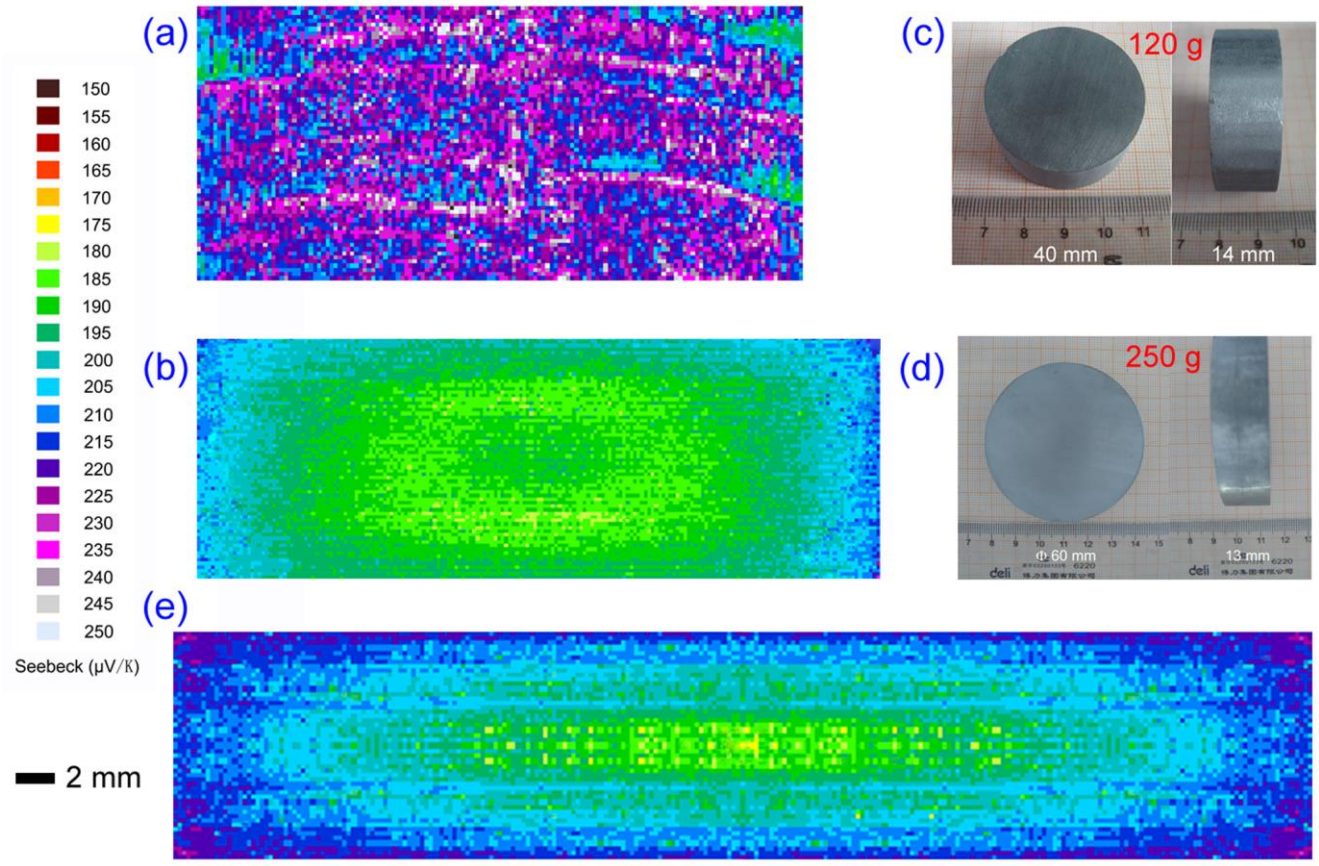

Figure 16. (a) Distribution of Seebeck coefficient values measured over the cross section of the ZM ingot; (b) distribution of Seebeck coefficient values measured over the cross section of the ingot with the diameter of 40 mm and height of 14 mm and sintered for 20 min; (c) images of an ingot with the diameter of 40 mm and height of 14 mm prepared by MS-PAS; (d) images of an ingot with the diameter of 60 mm and height of 13 mm prepared by MS-PAS; (e) distribution of Seebeck coefficient values measured over the cross section of the ingot with the diameter of 60 mm and height of 13 mm and sintered for 20 min.

This article is protected by copyright. All rights reserved.

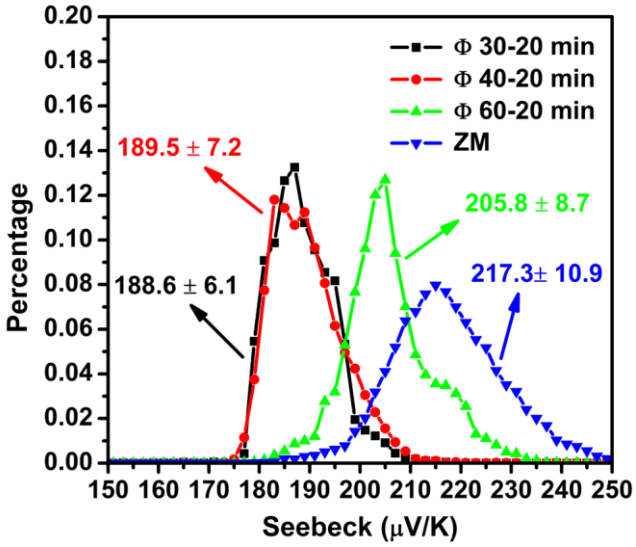

Figure 17. The statistical distribution of Seebeck coefficient for ingots sintering for 20 min and compared with the ZM sample, and the diameter of ingots is 30 mm, 40 mm, and 60 mm respectively.

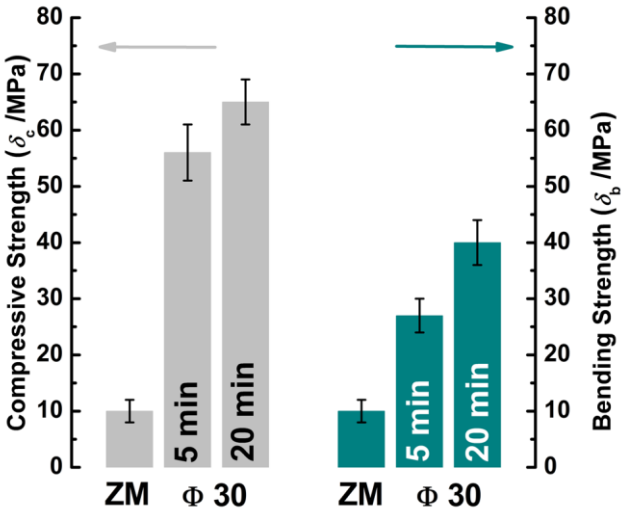

This article is protected by copyright. All rights reserved.

Figure 18. The compressive strength and the bending strength of samples cut from the ingot with the diameter of 30 mm and height of 12 mm and sintered for times of 5 min and 20 min, respectively. For comparison, the data for the ZM sample are also included.

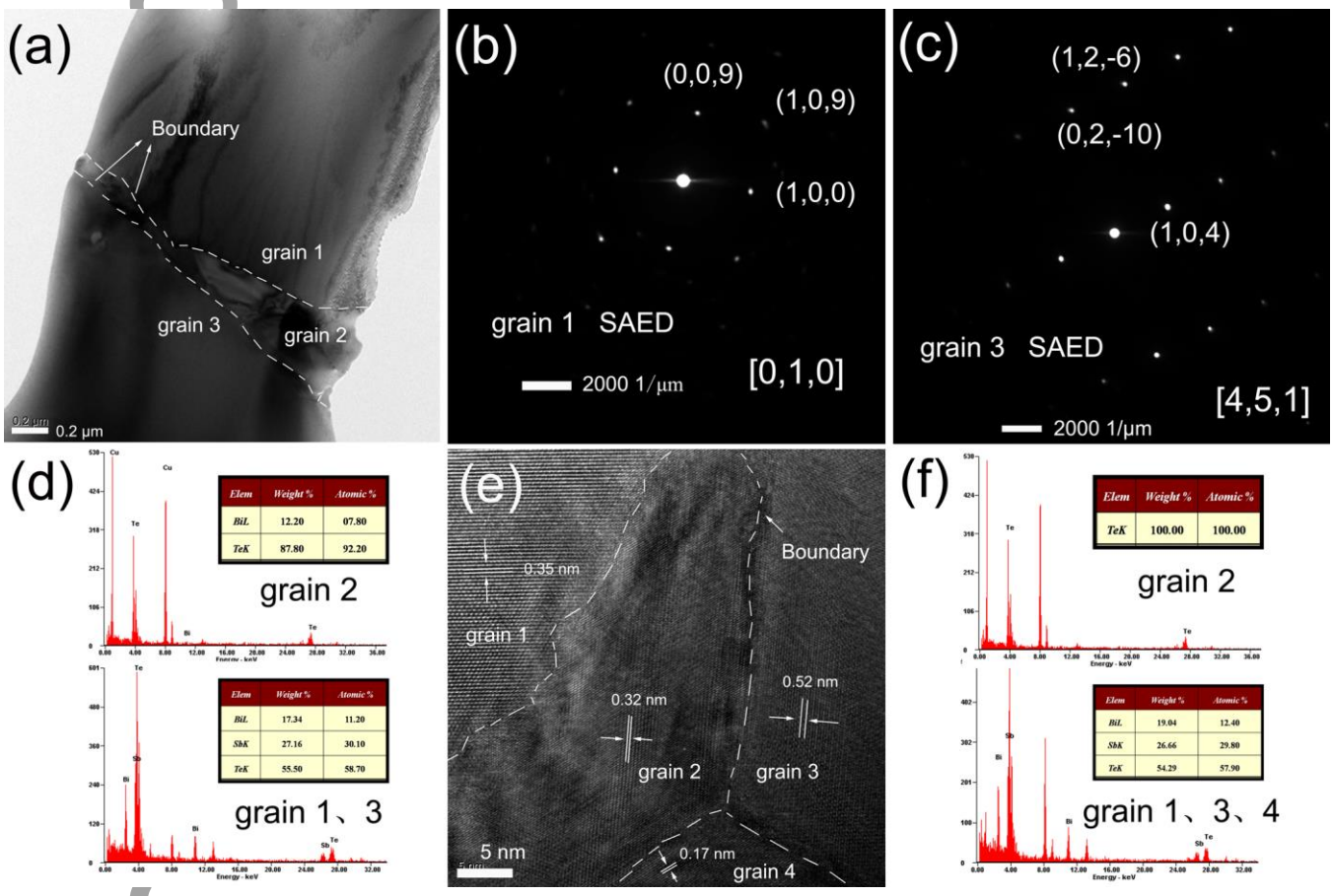

Figure 19. (a) TEM image of a sample cut from the ingot with the diameter of 30 mm and height of 12 mm and sintered for 5 min.; (b) SAED of grain 1 in Figure 19(a); (c) SAED of grain 3 in Figure 19(a); (d) EDS of grains 1, 2, and 3 in Figure 19(a); (e) HRTEM image of a sample cut from the ingot with the diameter of 30 mm and height of 12 mm and sintered for 20 min; (f) EDS of grains 1, 2, 3, and 4, in Figure 19(e).

This article is protected by copyright. All rights reserved.

This article is protected by copyright. All rights reserved.

Mechanically robust p-type Bi_2Te_3-based nanostructured bulk material in large size is prepared by melt-spinning combined with plasma activated sintering, which shows high thermoelectric performance together with excellent homogeneity. It is of critical importance for large-scale commercial applications of nanostructured thermoelectric materials, especially as it concerns the fabrication of thermoelectric micro-devices.

Thermoelectric, large-size, nanostructure, homogeneity

G. Zheng, X. L. Su,* X. R. Li, T. Liang, H. Y. Xie, X. Y. She, Y. G. Yan, C. Uher, M. G. Kanatzidis, X. F. Tang*

Toward high thermoelectric performance large-size nanostructured BiSbTe alloys via optimization of sintering temperature distribution

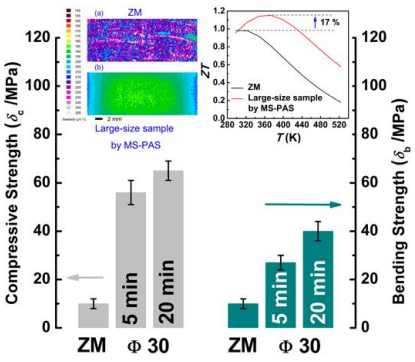

This article is protected by copyright. All rights reserved.

This article is protected by copyright. All rights reserved.